remote sensing

MDPI

Article

Snow Phenology and Hydrologic Timing in the Yukon River Basin, AK, USA

Caleb G. Pan [1,2,*], Peter B. Kirchner [3], John S. Kimball [2], Jinyang Du [2] and Michael A. Rawlins [4]

1 Innov8.ag Solutions, Walla Walla, WA 99362, USA
2 Numerical Terradynamic Simulations Group, W.A. Franke College of Forestry and Conservation, University of Montana, Missoula, MT 59801, USA; john.kimball@umt.edu (J.S.K.); jinyang.du@umt.edu (J.D.)
3 Southwest Alaska Network Inventory and Monitoring Program, National Park Service, Anchorage, AK 99501, USA; peter_kirchner@nps.gov
4 Department of Geosciences, University of Massachusetts, Amherst, MA 01003, USA; rawlins@geo.umass.edu
* Correspondence: caleb.pan@umt.edu

Abstract: The Yukon River basin encompasses over 832,000 km^2 of boreal Arctic Alaska and northwest Canada, providing a major transportation corridor and multiple natural resources to regional communities. The river seasonal hydrology is defined by a long winter frozen season and a snowmelt-driven spring flood pulse. Capabilities for accurate monitoring and forecasting of the annual spring freshet and river ice breakup (RIB) in the Yukon and other northern rivers is limited, but critical for understanding hydrologic processes related to snow, and for assessing flood-related risks to regional communities. We developed a regional snow phenology record using satellite passive microwave remote sensing to elucidate interactions between the timing of upland snowmelt and the downstream spring flood pulse and RIB in the Yukon. The seasonal snow metrics included annual Main Melt Onset Date (MMOD), Snowoff (SO) and Snowmelt Duration (SMD) derived from multifrequency (18.7 and 36.5 GHz) daily brightness temperatures and a physically-based Gradient Ratio Polarization (GRP) retrieval algorithm. The resulting snow phenology record extends over a 29-year period (1988–2016) with 6.25 km grid resolution. The MMOD retrievals showed good agreement with similar snow metrics derived from in situ weather station measurements of snowpack water equivalence ($r = 0.48$, bias = −3.63 days) and surface air temperatures ($r = 0.69$, bias = 1 day). The MMOD and SO impact on the spring freshet was investigated by comparing areal quantiles of the remotely sensed snow metrics with measured streamflow quantiles over selected sub-basins. The SO 50% quantile showed the strongest ($p < 0.1$) correspondence with the measured spring flood pulse at Stevens Village ($r = 0.71$) and Pilot ($r = 0.63$) river gaging stations, representing two major Yukon sub-basins. MMOD quantiles indicating 20% and 50% of a catchment under active snowmelt corresponded favorably with downstream RIB ($r = 0.61$) from 19 river observation stations spanning a range of Yukon sub-basins; these results also revealed a 14–27 day lag between MMOD and subsequent RIB. Together, the satellite based MMOD and SO metrics show potential value for regional monitoring and forecasting of the spring flood pulse and RIB timing in the Yukon and other boreal Arctic basins.

Keywords: snow cover; snowmelt; passive microwave; streamflow; Alaska

check for updates

Citation: Pan, C.G.; Kirchner, P.B.; Kimball, J.S.; Du, J.; Rawlins, M.A. Snow Phenology and Hydrologic Timing in the Yukon River Basin, AK, USA. *Remote Sens.* **2021**, *13*, 2284. https://doi.org/10.3390/rs13122284

Academic Editor: Annett Bartsch

Received: 9 May 2021
Accepted: 8 June 2021
Published: 10 June 2021

Publisher's Note: MDPI stays neutral with regard to jurisdictional claims in published maps and institutional affiliations.

Copyright: © 2021 by the authors. Licensee MDPI, Basel, Switzerland. This article is an open access article distributed under the terms and conditions of the Creative Commons Attribution (CC BY) license (https://creativecommons.org/licenses/by/4.0/).

1. Introduction

Annual hydrologic variability in snowmelt dominated basins is reflected in snow cover dynamics [1]. Several studies in the western United States found warming temperatures promoted an earlier snowmelt onset and subsequent runoff [2–4]. The earlier onset of snowmelt can slow the rate of melt due to less early season incoming solar radiation [5] while proportionally reducing annual streamflow [1]. However, seasonal trends toward earlier snowmelt and longer melt durations and the associated impacts on snowmelt driven flooding and river ice break up (RIB) patterns remain relatively uncertain [6,7].

Snowmelt is the primary discharge component to river and stream networks across the boreal Arctic and important to the timing of the spring flood pulse and RIB, which in turn affects flood risk and navigational hazards along the Yukon River and its tributaries [8]. The Yukon River, a linchpin for Arctic communities and people residing along its banks, provides a primary travel route and opportunities for fishing and other subsistence resources [9]. Changes in the timing of the Yukon River spring flood pulse and summer flows can impact the river fluvial dynamics and erosion, influencing water quality, regional infrastructure and travel [10]. Upland conditions, including snow depth and the timing of snowmelt in spring, play an important role in downstream RIB which can lead to ice-jam floods and serious threats to downstream communities [11].

Significant changes in the snow phenology of the Yukon basin and wider boreal Arctic are occurring and projected to continue due to the polar amplification of global warming [12,13]. These changes will affect the regional climate, human activities, ecosystem services, and hydrologic processes. Better monitoring and understanding of the spatiotemporal variability in seasonal snowmelt is critical for assessing risk and for mitigating potential adverse impacts on Alaskan communities [10]. However, capabilities for regional monitoring and observations of the patterns and trends in snowmelt processes is limited in the Yukon and other boreal Arctic regions due to the sparse and discontinuous observations of climate, discharge and ice conditions, and the vast geographic domain of the region [14,15]. Remote sensing observations from polar orbiting satellites have global coverage and frequent sampling over the boreal Arctic and provide an opportunity to observe snow processes at moderate resolution. Passive microwave observations, in particular, are useful because brightness temperature measurements from both lower frequency (1–2 GHz) and higher frequency (18–37 GHz) radiometers are highly sensitive to liquid water content (LWC) changes within the snowpack [16–18]. Further, clouds and polar darkness have little influence over the passive microwave (PMW) retrievals due to the high atmospheric transparency to land surface microwave emissions at these frequencies, which do not rely on incoming solar energy [19]. Additionally, calibrated brightness temperature records developed from similar sensors on successive satellite missions provide approximately twice-daily sampling suitable for monitoring snowmelt dynamics with continuous and relatively long-term records suitable for evaluating environmental trends.

Several different algorithms have been found useful for detecting snowmelt processes. These algorithms exploit the sensitivity of PMW frequencies and polarizations to snow surface conditions and have been developed using twice-daily (ascending and descending orbit) PMW brightness temperature (Tb) acquisitions from polar orbiting environmental satellites. The algorithm types include: (i) Tb diurnal amplitude variation [20,21], (ii) brightness temperature (Tb) differencing approach [22], (iii) single frequency coupled with reanalysis surface temperatures [23] and (iv) the gradient ratio polarization (GRP) approach [24,25].

Several snow phenology metrics have been derived from PMW retrievals and associated algorithms for mapping and monitoring purposes. As described here, the Mean Melt Onset Date (MMOD) is an indicator of springtime snow surface wetness prior to the onset of an isothermal snowpack and the associated spring snowmelt discharge pulse. The Snowoff (SO) date, or last day of significant snow cover, corresponds with the relatively abrupt shift in land surface albedo between the predominantly snow-covered winter season and the start of the growing season [26–28]. Hence, the difference between SO and MMOD defines the Snowmelt Duration (SMD) [8,29,30], an important indicator of spring phenology, regional hydrology and RIB [5,31].

The goal of this paper is to elucidate the spatiotemporal relationships between seasonal snow properties, ice breakup dynamics and discharge in the Yukon River Basin (YRB) using a new PMW satellite-derived snowmelt record of MMOD, SO, and SMD from 1988–2016. Our objectives are to: (1) validate the PMW derived MMOD metric using in situ climate observations and elucidate the roles of fractional water inundation, forest cover, and terrain on MMOD retrieval uncertainty; (2) quantify regional variation in the selected snowmelt

properties over the YRB and (3) describe the leading snowmelt contributors to the spring flood pulse and RIB for the major YRB tributaries.

2. Materials and Methods

2.1. Study Domain

The Yukon River traverses east to west and, along with its tributaries, constitutes one of North America's largest river basins. This region experiences six to nine months of snow cover annually, and spring snowmelt runoff is the main hydrologic contribution to the system [10]. The YRB has a mean annual discharge of 6400 m^3 s^{-1}, a drainage area exceeding 853,300 km^2 [8,29] and covers 10 degrees of latitude from 59°N to 69°N, extending into the Canadian Yukon and British Columbia to the east, and reaching the Alaska Bering Sea coast to the west. The diverse topography, with a median elevation of 617 m and extending from sea level to the highest elevations of the Brooks (2735 m) and Alaska (6190 m) Ranges, encompasses a diversity of northern boreal, arctic, alpine and maritime biomes. Evergreen needleleaf forests are the dominant vegetation cover (54%) followed by broadleaf deciduous forests (9%) covering the valley bottoms and into the mid-elevations. The Yukon Delta and higher elevations have tall and low shrubs (9%) mixed with some dry and wet herbaceous (9%) tundra as the dominant plant community. Permafrost is present to a large extent in the YRB, and comprises several types including sporadic (14%), discontinuous (46%) and continuous (16%) and moderately thick to thin permafrost (24%) [32].

We constrained our analysis of the YRB to three major catchments defined by the location of reliable long-term gauging stations located on main stem of the Yukon River. Catchment distributions within the YRB are shown in Figure 1, including Eagle (287,800 km^2), Stevens Village (500,968 km^2) and Pilot (817,961 km^2), in order of catchment size.

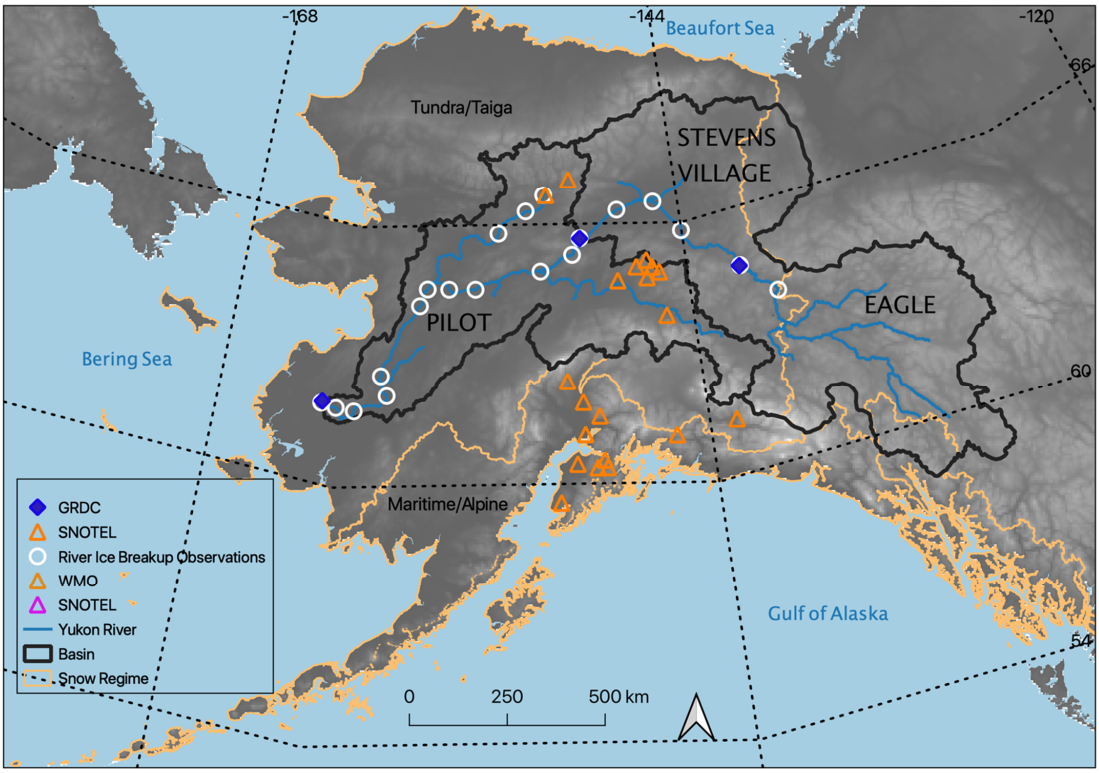

Figure 1. The spatial extent of the 1988–2016 MMOD, SO and SMD snow data shown along with GRDC gauging stations (blue diamonds), catchment outlines in black, river ice breakup observations (white circles) and SNOTEL locations (orange triangles). Base map provided from GTOPO.

2.2. Passive Microwave Satellite Record 1988–2016

The detection of MMOD and SO used the 19 and 37 GHz afternoon Tb retrievals at horizontal (H) and vertical (V) polarizations from the MEaSUREs Calibrated Enhanced-Resolution Passive Microwave Daily EASE-Grid 2.0 Brightness Temperature ESDR, available at the National Snow and Ice Data Center [33].This multidecadal data record represents Tb retrieval records calibrated across multiple sensors and platforms for different frequencies and polarizations from the NOAA DMSP Special Sensor Microwave/Imager (SSM/I) and the Special Sensor Microwave Imager/Sounder (SSMIS) [34]. Each platform has several sensors. When using SSM/I, we used DMSP-F8 (1987–1991), DMSP-F10 (1992–1997), and DMSP-F13 (1997–2005). For missing temporal observations, we gap-filled using overlapping sensors. For the later years, DMSP-F15 and DMSP-F18 provided the bulk of observations from 2000–2010 and 2010–2016, respectively. Missing temporal observations were again gap-filled with overlapping observations from other sensors.

The sampling resolution of the combined 19 and 37 GHz Tb retrievals are ~ 25 km or coarser; however, the MEaSUREs products used for this study were processed using the scatterometer image reconstruction approach to obtain an enhanced spatial grid resolution of 6.25 km (19 GHz) and 3.125 km (37 GHz) from the overlapping Tb antenna patterns [34,35]. To establish a continuous record, 3.125 km 37 GHz retrievals were resampled to 6.25 km using a nearest neighbor interpolation, and missing grid cells were gap-filled using a temporal linear interpolation of adjacent Tb retrievals [22].

2.3. Other Ancillary Datasets

We used composited weekly FW time series from a regional AMSR (Advanced Microwave Scanning Radiometer) FW record [36] to derive a mean summer (JJA) fractional water (FW) map for the AMSR period of record (2002 to 2016). The resulting static FW map was used to define where water bodies persist across the landscape and areas where the PMW land retrievals may be influenced by surface water contamination. We used glacier outlines acquired from the Global Land Ice Measurements from Space (GLIMS) program to identify and mask out SO dates and SMD grids from statistical analysis for regions in Alaska that have snow and ice year-round. We also used the Fractional Forest (FF) cover (%) from the MODIS (Moderate Resolution Imaging Spectroradiometer) MOD44B land cover product [37] to assess the influence of vegetation cover on the relative accuracy of the snowmelt metrics. The 250 m resolution MOD44B data were reprojected to match the 6.25 km PMW grid using nearest-neighbor resampling.

Monthly gridded surface air temperatures were obtained for the YRB from the Weather Research and Forecasting (WRF) Reanalysis, downscaled to 20 km using ERA-Interim historical reanalysis data (1979–2015) acquired from the Scenarios Network for Alaska and Arctic Planning (SNAP) [38]. We used nearest-neighbor interpolation to resample monthly average temperatures to the 6.25 km PMW grid. Resampled annual monthly temperature grids were then used to produce correlations with the annual snowmelt metrics. A complete list of the primary datasets used in this study is found in Table 1.

Table 1. Datasets used in this study. See Appendix E for abbreviations.

Dataset	Spatial Resolution	Period of Record	Use	Reference/Source
PMW	6.25 km	1988–2016	MMOD	Brodzik et al. 2018
Snowoff	6.25 km	1988–2016	SO, SMD Analysis	Pan et al. 2020
FW	6.25 km	2003–2015	MMOD/Validation	Du et al. 2017
FF	250 m	2011	Validation	Carroll et al. 2011
WRF Reanalysis	20 km	1988–2015	Climate Analysis	SNAP UAF
SNOTEL	in situ	2004–2016	Validation	NRCS
Streamflow	in situ	1988–2016	Streamflow Analysis	GRDC
River Ice Observations	in situ	1988–2016	RIB Analysis	NWS

2.4. Deriving MMOD

We used a Tb spectral gradient ratio polarization (GRP) [24,39] and a Tb differencing approach [40] to detect MMOD (henceforth we denote the PMW derived snow metrics as $MMOD_{PMW}$, SO_{PMW}, and SMD_{PMW}). The GRP algorithm detects the $MMOD_{PMW}$ within a given grid cell and annual (water year) time series when the GRP running mean (*rm*) is less than the difference between the water year's average winter (January–March) GRP (*win*) and an input melt parameter threshold, *param* (Figure 2). Here, *param* is a dynamic variable that ranges from 0.2 to 0.6 and determines how low the GRP must be relative to *win* for the $MMOD_{PMW}$ to be detected. The duration of the *rm* and *param* are spatially dependent on an ancillary static surface FW map. In general, we found the GRP snow signal to be degraded for grid cells with higher FW cover. However, the GRP derived $MMOD_{PMW}$ performance was improved by assigning a higher *param* value for cells with higher water coverage below a 39% FW threshold, while the *param* value was set at 0.2 for higher FW levels above this threshold. For certain years and locations, the GRP algorithm was unable to detect the $MMOD_{PMW}$ and for these grid cells we used the Tb difference between the 19V and 37V channels for the $MMOD_{PMW}$ classification [22,40].

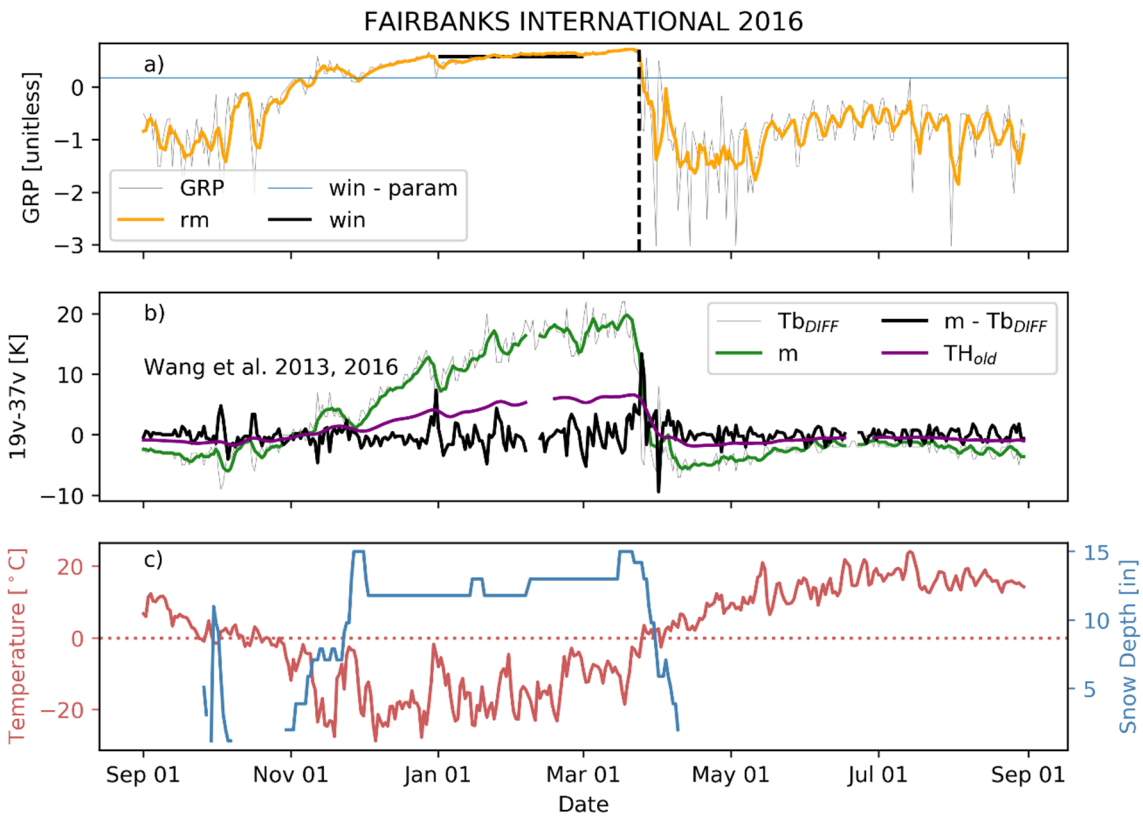

Figure 2. 2016 water year at Fairbanks, Alaska (64°48′59″N, 147°51′49″W): (**a**) daily GRP values (grey); four-day GRP running mean (*rm*), (orange); mean GRP value from 1 January to 1 March (*win*) (black); threshold value derived from subtracting the winter mean GRP (*win*) and FW melt threshold parameter (param) (horizontal blue line). (**b**) MMOD detection algorithm outlined in [22]. (**c**) Daily average air temperature and snow depth.

The Tb difference algorithm requires the derivation of three variables, including the daily difference between 19V–37V (Tb_{DIFF}), previous three-day average of Tb_{DIFF} (m), and the product of m multiplied by an empirical constant, 0.35 (TH_{old}). When the difference between m and Tb_{DIFF} exceeds TH_{old} for four or more days, this indicates the MMOD (Figure 2b). More information on this algorithm is outlined in [22].

SO_{PMW} was derived using the 19V–37V Tb differencing approach, which exploits varying sensitivity of the different Tb frequencies to surface scattering, wetness and dielectric properties between snow-covered and fully ablated landscapes [25]. The Tb difference

is positive and relatively stable prior to the seasonal onset of snowmelt, but as the snow begins to ablate the Tb difference precipitously decreases, mirroring the snow ablation rate before reaching a seasonal minimum. The Tb difference reaches a seasonal minimum just after the snowpack has largely ablated, which we use to represent the SO_{PMW} condition. SMD_{PMW} is then derived by taking the difference between the SO_{PMW} and $MMOD_{PMW}$, resulting in the number of days required for the snowpack to melt out for a given grid cell.

2.5. MMOD Validation and Evaluation

The $MMOD_{PMW}$ metric was validated using daily Snow Water Equivalent (SWE) and air temperature measurements at 20 Alaska SNOw TELemetry (SNOTEL) network stations (Appendix A). At each SNOTEL station, we calculated the site-level MMOD using both SWE ($MMOD_{SWE}$) and temperature ($MMOD_T$) measurements and compared these measurements to the collocated satellite based $MMOD_{PMW}$ retrieval. Each local station MMOD was derived using an eight-day forward moving window temporal mean of the daily SWE measurements to extract the date where SWE was at its peak, with the assumption that depletion after this date corresponds with a melting snowpack (Figure 2). Each alternative temperature derived $MMOD_T$ was calculated using an eight-day rolling mean of daily air temperature measurements at each station, where the MMOD was defined as the first date where the mean air temperature exceeded 0 °C. Both the SWE and air temperature derived MMOD definitions infer the shift in the seasonal energy budget that initializes snowmelt [41]. The relative accuracy of the $MMOD_{PMW}$ retrievals was assessed against the SNOTEL site-based MMOD observations using bias and correlation as measures of performance. The $MMOD_{PMW}$ record was also compared against a spatially continuous annual record of primary spring thaw timing derived from a daily Freeze/Thaw (FT) classification of SSM/I 37V GHz Tb retrievals spanning the same domain and multiyear record as the current study but derived at a coarser 25 km spatial resolution [23].

2.6. Snow and Streamflow Indices in the Yukon River Basin

The differences in timing between upland snowmelt and basin streamflow were examined across a selection of regional catchments within the larger YRB. Daily streamflow data were obtained from the Global Runoff Database Centre (GRDC) for three major river gaging stations located along the Yukon River main stem at Eagle, AK (64.79, −141.20), Stevens Village, AK (65.88, −149.72) and Pilot Station, AK (61.93, −162.88); the three stations are located at the outlets of the major YRB catchments, representing respective drainage areas of 287,800 km^2, 500,969 km^2, and 817,962 km^2. Except for the years 1997–2002 at Pilot, all stations had complete streamflow data records spanning the study period (1988–2016).

Streamflow timing indices were represented as Q20, Q50, and Q80 terms calculated as the respective days of the year (DOY) when 20, 50 and 80% of the total annual (WY) flow passed the station gage location [2,3]. We also extracted the DOY representing the peak annual discharge at each station (Figure 3). Snowmelt indices were also represented from the PMW record as quantiles but calculated as the DOY when 20, 50 and 80% of the cumulative catchment area [%] above each streamflow station was either under active snowmelt or snowoff conditions. We represented the cumulative area of snowmelt contributing to the measured discharge for each basin as the difference between the cumulative catchment area under respective melt and snowoff conditions (denoted as *contributing* in Figure 4). Discharge and snowmelt indices were extracted for each year and station location. Least-squares linear regression was used to quantify the relationship between the streamflow (dependent) and snowmelt (independent) indices to determine how much streamflow variability could be explained by the level of snowmelt activity. The resulting regressions were also used to identify any apparent lead time between the PMW derived catchment snow metrics and the subsequent downstream flood pulse indicated from the catchment discharge measurements.

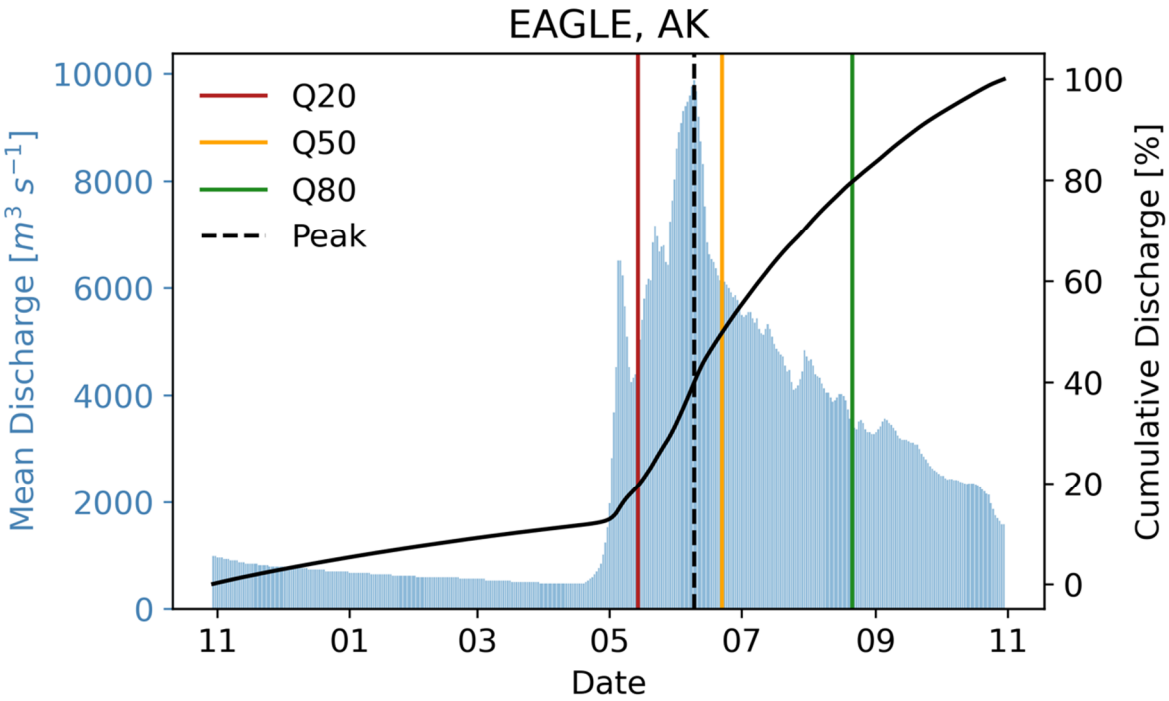

Figure 3. Observed mean daily streamflow at Eagle, AK during selected WY 1993. The Y2-axis shows the cumulative discharge [%] and was used to identify the temporal Q20 (red), Q50 (orange), and Q80 (green) discharge thresholds. The DOY of peak discharge is denoted by the dashed black line.

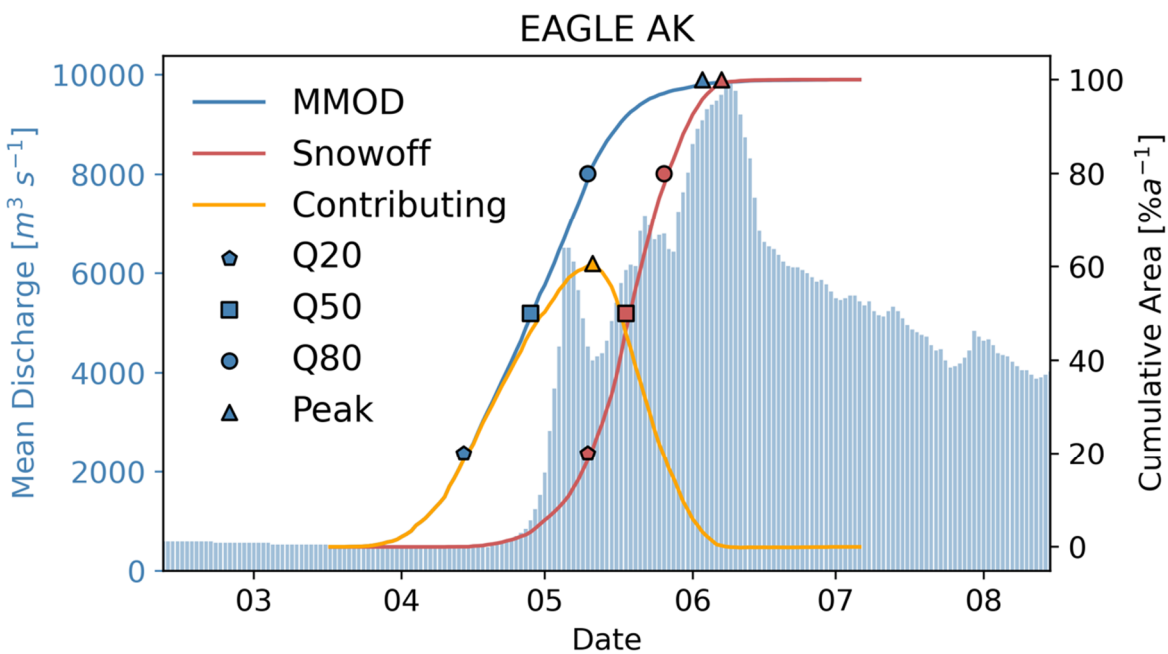

Figure 4. Mean daily discharge at Eagle, AK during selected WY 1993. The Y2-axis shows the cumulative catchment area [%] that has begun to melt ($MMOD_{PMW}$) or experienced snowoff (SO_{PMW}) indicated from the satellite record. The orange line is the difference between $MMOD_{PMW}$ and SO_{PMW} and indicates the proportional area of active snowmelt contributing to streamflow.

2.7. Snow and River Ice Breakup in the Yukon River Basin

We next examined the interaction between the timing of upland snowmelt and seasonal river ice breakup within the YRB. RIB observations were acquired for 19 station locations (Figure 1) along the Yukon River main stem from the National Weather Service's Historical River Observations Database (www.weather.gov/aprfc/rivobs, Accessed: November 1, 2020). The number of annual RIB observations ranged from 18 to 28 years with a mean record length of 24 years from 1988 to 2016. All river ice observation locations used in this study are listed in Appendix B.

We again used linear regression analysis to quantify the relationship between annual RIB date and the snowmelt indices within each catchment. However, unlike the discharge analysis involving three major sub-basins, the river ice analysis encompassed a larger number of catchments associated with the more extensive RIB station network. Similar snow metric quantiles were calculated for the upstream catchments associated with each RIB station location. For snowmelt metrics that were statistically significant ($p < 0.05$), we then calculated the average annual difference (i.e. temporal lag) between the mean timing (DOY) of a given catchment snowmelt metric and the associated RIB date.

3. Results

3.1. MMOD Classification Accuracy

The $MMOD_{PMW}$ results were generally consistent with the primary spring thaw onset indicated from the coarser (25 km resolution) FT-ESDR product [23]. In both datasets, MMOD/Spring Onset typically occurs later in the Alaska North Slope and at higher elevations (Figure 5). The mean $MMOD_{PMW}$ in the YRB from 1988–2016 was DOY 113 (±11 days; temporal SD), while the FT-ESDR Spring Onset mean was DOY 108 (± 7 days) for the same period. Thus, $MMOD_{PMW}$ typically occurs about five days later than the FT-ESDR spring onset and has higher spatial (SD) heterogeneity attributed to the spatially enhanced Tb record used for the $MMOD_{PMW}$ retrievals. The $MMOD_{PMW}$ pattern also appears to better preserve the influence of the regional topography and land cover on spring melt timing, as described in the following sections.

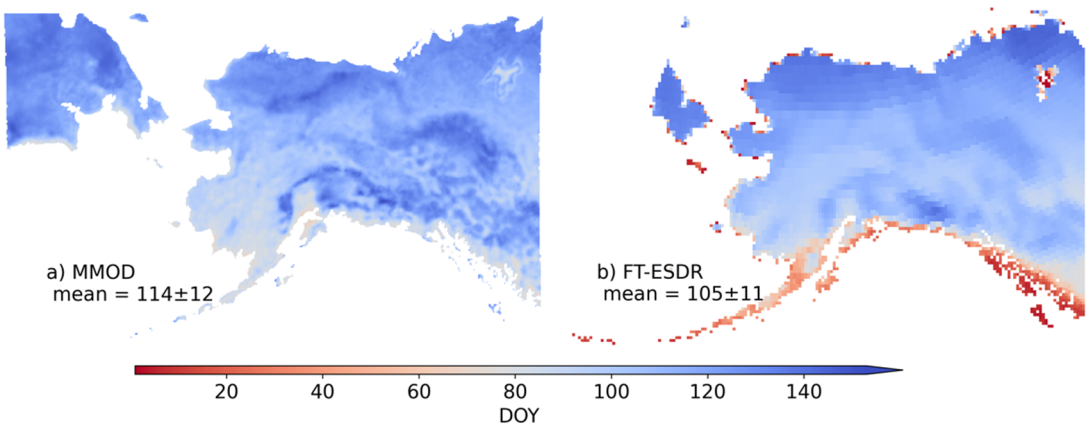

Figure 5. (**a**) Mean annual $MMOD_{PMW}$ from 1988–2016 at 6.25 km resolution, compared with the (**b**) PMW-derived mean annual Spring Onset timing from the 25 km resolution FT-ESDR product for the same period. * The mean and standard deviations correspond to the entire dataset.

The mean correlation between the satellite $MMOD_{PMW}$ retrievals and in situ MMOD estimates derived from SNOTEL station SWE measurements ($MMOD_{SWE}$) was 0.49 with a bias of −3.63 days, indicating an earlier $MMOD_{PMW}$. The mean correlation between $MMOD_{PMW}$ and the in situ air temperature measurement-based MMOD estimates ($MMOD_T$) was stronger (0.69) and showed a smaller (~1 day) bias. Aggregation of the correlation results by snow cover classification [39] showed generally stronger $MMOD_{PMW}$ mean correspondence in the colder Tundra/Taiga snow regime with the respective SNOTEL

SWE and air temperature-based MMOD observations (0.62 and 0.81). The MMOD mean correlations were generally lower for Alpine/Prairie (0.31 and 0.61) and Maritime (0.35 and 0.41) snow regimes.

For each of the three snow classification zones, we investigated the influence of different landscape factors on the relative bias between the $MMOD_{PMW}$ retrievals and the SNOTEL $MMOD_{SWE,T}$ observations, including FW cover; fractional forest (FF) cover; terrain aspect and elevation, and topographic roughness index (TRI). In the Tundra/Taiga region, the $MMOD_{PMW}$ and $MMOD_{SWE}$ bias was moderately correlated with FF ($r = -0.61$, $p < 0.1$) and moderately correlated with FW ($r = -0.86$, $p < 0.1$) within a surrounding grid cell. In contrast, the $MMOD_{PMW}$ and $MMOD_{T}$ bias corresponded more strongly with terrain aspect northness ($r = -0.87$, $p < 0.1$). In the Alpine/Prairie region, $MMOD_{PMW}$ and $MMOD_{SWE}$ biases were strongly influenced by elevation ($r = 0.92$, $p < 0.1$) and TRI ($r = 0.94$, $p < 0.1$), whereas the $MMOD_{PMW}$ and $MMOD_{T}$ biases were only influenced by FW ($r = 0.99$, $p < 0.1$). In the Maritime region, $MMOD_{PMW}$ and $MMOD_{SWE}$ biases were influenced by FW ($r = -0.74$, $p < 0.1$), whereas the $MMOD_{PMW}$ and $MMOD_{T}$ biases were influenced by FW ($r = -0.77$, $p < 0.1$) and aspect northness ($r = -0.68$, $p < 0.1$). These results indicate that enhanced surface moisture influences the agreement between the $MMOD_{PMW}$ and SNOTEL observations, as the 37 GHz Tb observations are strongly sensitive to surface water within the satellite footprint [23]. The influence of FF cover particularly in the boreal interior regions was demonstrated, as microwave emissions from surface snow cover can be adversely affected by the overlying forest cover at both 19 and 37 GHz frequencies [42].

3.2. Snow Metric Distribution in the YRB

The average snow metric spatial distribution (1988–2016) indicated a topographic influence with generally earlier (later) $MMOD_{PMW}$ and SO_{PMW} at lower (higher) elevations. The PMW record also showed significant interannual variability in the spring snow metrics, indicated by the extensive early spring onset during the exceptionally warm year of 2016 relative to a more climatological normal year in 2001. The SMD_{PMW} distribution showed relatively less spatial and annual variability but a longer duration of spring snowmelt in the YRB upper headwaters and lower delta regions (Figure 6).

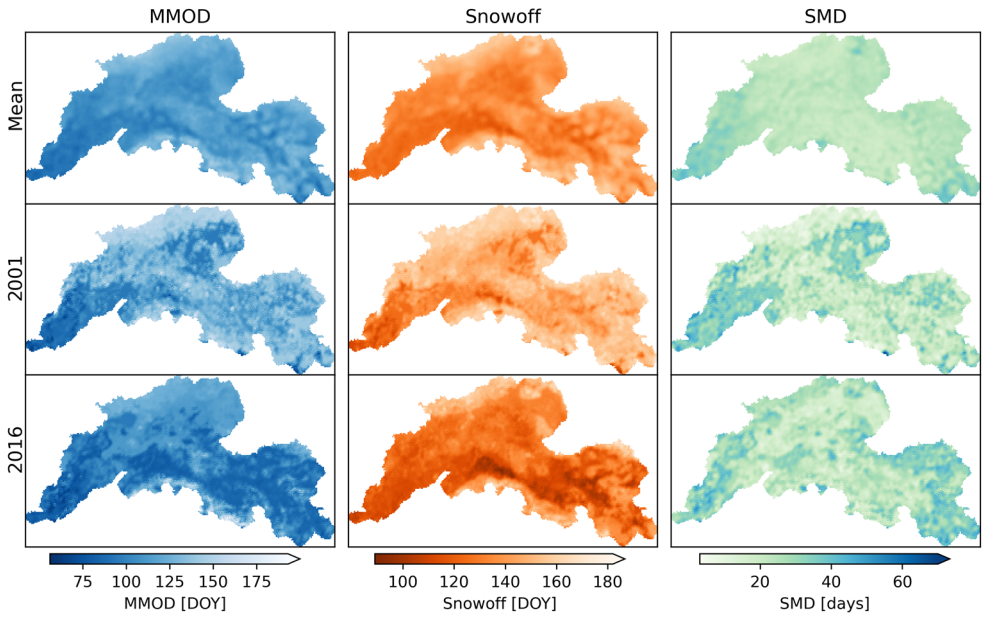

Figure 6. The snow metrics spatial distribution in the YRB. The top row is the average value established from the long-term satellite record (1988–2016), the middle row is the spatial distribution for a climatologically normal year (2001) and the bottom row is the spatial distribution for an exceptionally warm year (2016).

On average, $MMOD_{PMW}$ in the YRB ranged from DOY 82 at lower elevations to DOY 153 at higher elevations, with a regional mean of DOY 113 ± 12. Alaska experienced record-setting warmth during the 2015/16 snow season (October–April), with statewide temperatures 4 °C above the mean [43]. During this year, the average $MMOD_{PMW}$ in the YRB was DOY 101 ± 16, which was 12 days earlier than the long-term mean (1988–2016) and 22 days earlier than in 2001.

SO_{PMW} in the YRB on average ranged from DOY 116 to 162 between lower and higher elevations, with a regional mean value of DOY 138 ± 9. Like $MMOD_{PMW}$, SO_{PMW} showed a regional mean of DOY 127 ± 13 during the exceptionally warm year in 2016, which was approximately 11 days earlier than normal relative to the long-term mean (1988–2016), and 20 days earlier than in 2001.

The average spring SMD_{PMW} in the YRB ranged spatially from 16 to 42 days, with a regional average of 25 ± 4 days over the long-term record. SMD_{PMW} appeared to have a less distinct spatial distribution relative to $MMOD_{PMW}$ and SO_{PMW}, but with longer durations in the YRB upper headwater and delta regions. A longer SMD_{PMW} occurred during the unprecedented warm year in 2016 (26 ± 8 days) relative to 2001 (24 ± 9 days). The longer duration in 2016 is in line with other studies that identified a lengthening snowmelt season under warming conditions [44,45].

The spatial distribution of correlations between the snow metrics and annual May temperatures are shown in Figure 7. Here, we quantified the relationship between annual snow metrics and temperature using monthly aggregated air temperatures from the downscaled (20 km resolution) WRF Reanalysis (Table 2). Overall, all spring snow metrics showed generally significant but variable correlations with May temperatures in both sign and magnitude. $MMOD_{PMW}$ and temperature regressions conducted within 100 m elevational bins showed lower elevations having the greatest percentage of significant ($p < 0.1$) grid cells, ranging from 51–60% over the 0–700 m elevational range, with moderate correlations (−0.41 to −0.44). The strongest correlations occurred at higher elevations (1200–1600 m) and ranged from −0.45 to −0.47, although the area of significant grid cells was lower (30%). Overall, $MMOD_{PMW}$ had a significant relationship with temperature for 42% of the YRB, respectively.

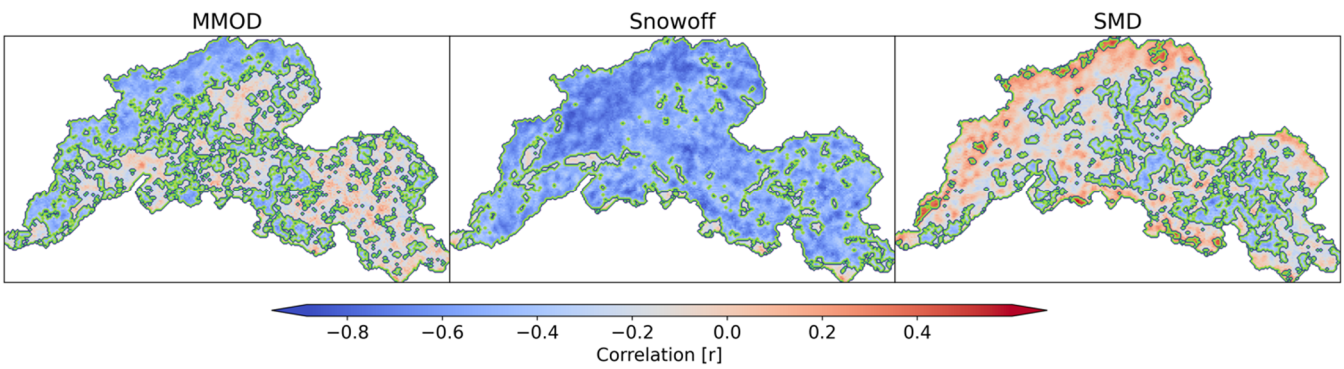

Figure 7. The correlation between May annual temperature and MMOD (**left**), SO (**middle**) and SMD (**right**). The green contour lines indicate areas with significant relationships ($p < 0.1$).

The SO_{PMW} correlations with May temperatures showed significant relationships over 60 to 85 percent of the area at elevations below 1000 m in the YRB with correlations ranging from −0.40 to −0.57. The number of grid cells with significant SO_{PMW} and spring temperature relationships were lower at higher elevations (1100–3000 m), with correlations ranging from −0.30 to −0.52. The SO_{PMW} relationship with temperature was also predominantly negative over 87% of the YRB, indicating generally earlier (delayed) snowpack depletion in warmer (cooler) years.

Table 2. Snow metrics and discharge regressions summary table including significant interactions and correlations. All regression outputs are found in Appendix C.

Snow Variables	Correlation [r]			Significant Variables	Basin
	Mean	Minimum	Maximum		
MMOD Q20	0.5	0.5	0.5	['Q20 ']	EAGLE
SO Q20	0.61	0.61	0.61	['Q20 ']	EAGLE
Contribution Peak	0.6	0.6	0.6	['Q20 ']	EAGLE
MMOD Q80	0.68	0.65	0.71	['Peak', 'Q20']	STEVENS VILLAGE
SO Q50	0.675	0.64	0.71	['Peak', 'Q20']	STEVENS VILLAGE
SO Q80	0.59	0.52	0.66	['Peak', 'Q20']	STEVENS VILLAGE
MMOD Q50	0.41	0.4	0.42	['Peak', 'Q20']	PILOT
MMOD Q80	0.49	0.4	0.58	['Peak', 'Q20']	PILOT
SO Q20	0.5	0.48	0.52	['Peak', 'Q20']	PILOT
SO Q50	0.59	0.55	0.63	['Peak', 'Q20']	PILOT

The SMD_{PMW} relationship with May temperatures was relatively spatially complex due to the variable influence of temperature on $MMOD_{PMW}$ and SO_{PMW}. SMD_{PMW} was significantly correlated with temperature over 75% of the YRB, but with both positive and negative relationships for 22% and 53% of the domain, respectively. The positive SMD_{PMW} temperature response was predominantly located at higher elevations (>800 m) characterized by deeper snowpack conditions [46].

3.3. Streamflow and River Ice Breakup

3.3.1. Interaction between Snow Metrics and Discharge in the YRB

We iterated through 36 regressions for Eagle, Stevens Village and Pilot sub-basins. Regressions included quantiles (Q20, Q50, Q80) for each snow metric (MMOD, SO, and SMD) defined as the percent area of a catchment regressed against streamflow quantiles (Q20, Q50, Q80, and Peak), defined as the percent of cumulative annual flow at each gaging station. At the Eagle station, statistically significant ($p < 0.1$) regressions were observed only for the timing of $MMOD_{PMW}$ quantiles ($Q20_{MMOD}$, $Q50_{MMOD}$, and $Q80_{MMOD}$) and streamflow $Q20_{Flow}$. Regressions were also significant for the same SO quantiles ($Q20_{SO}$, $Q50_{SO}$, and $Q80_{SO}$) and streamflow $Q20_{Flow}$ (Appendix C). For MMOD, $Q20_{MMOD}$ had the highest correlation with the observed $Q20_{Flow}$ ($r = 0.5$) followed by $Q50_{Flow}$ (0.48) and $Q80_{Flow}$ (0.47). SO_{PMW} regressions were higher relative to $MMOD_{PMW}$, with $Q20_{SO}$ having a moderately strong correlation of 0.61 with $Q20_{Flow}$, suggesting a stronger relationship between SO_{PMW} and streamflow compared to $MMOD_{PMW}$ at Eagle (Table 2).

Moving downriver from Eagle to Stevens Village, we found overall relationships strengthened between the $MMOD_{PMW}$ and SO_{PMW} quantiles, and streamflow. At Stevens Village, the regressions showed significant relationships between the snow metric quantiles and $Q20_{Flow}$ in addition to peak flow. The timing of $Q80_{MMOD}$ correlated well with the timing of the hydrologic peak ($r = 0.71$). Moreover, the timing of $Q50_{SO}$ and $Q80_{SO}$ were also strongly correlated with the timing of the hydrologic peak, with respective correlations of 0.71 and 0.66. We also found a strong relationship between $Q20_{SO}$ and the $Q20_{Flow}$ ($r = 0.68$) at Stevens Village.

At the Pilot gaging station, $Q20_{MMOD}$ no longer showed a significant relationship with streamflow. However, $Q50_{MMOD}$ and $Q80_{MMOD}$ were still moderately correlated with the timing of the streamflow peak, with respective correlations of 0.42 and 0.58. The SO_{PMW} quantiles and the streamflow quantiles remained stronger than for $MMOD_{PMW}$, with $Q20_{SO}$ and $Q50_{SO}$ having correlations of 0.52 and 0.63 with the timing of the peak flow. Overall, $Q20_{SO}$ had the highest correlation with $Q20_{Flow}$ at the Eagle station. However, for Stevens Village and Pilot stations, $Q50_{SO}$ had the strongest relationship with the timing of the streamflow peak. For the 1988 to 2016 record, $Q50_{SO}$ occurred, on average, 16 ± 16 days earlier than the streamflow peak at Eagle; the lag time was less at Stevens Village (9 ± 10 days) and longer at the Pilot (17 ± 9 days) station (Figure 8).

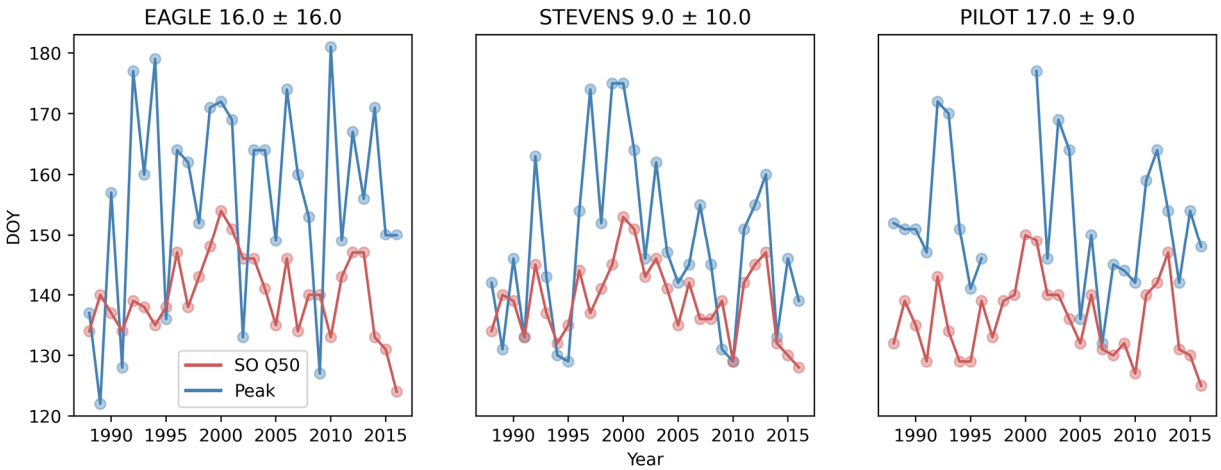

Figure 8. Differences between annual timing of the satellite PMW-derived catchment $Q50_{SO}$ quantile (red) and the hydrologic peak (blue) from 1988–2016 for Eagle, Stevens Village, and Pilot gaging stations.

Overall, there is an initial influence of snow processes on discharge at the higher reaches, represented by Eagle. Snowmelt had a stronger influence on discharge in the middle YRB reaches at Stevens Village. Moving to Pilot, larger MMOD quantiles (Q50, Q80) influenced the peak flow but to a lesser degree relative to $Q20_{SO}$ and $Q50_{SO}$.

3.3.2. Interaction between Snow Metrics and River Ice Breakup in the YRB

We examined the interaction between the satellite PMW-derived annual snow metrics and observed RIB dates using snow metric pixel values at 19 RIB measurement locations along the Koyukuk and Yukon rivers. Significant relationships ($p < 0.1$) between $MMOD_{PMW}$ and RIB were identified at 11 of the 19 locations (Figure 9). The strongest relationships were found at Beaver (r = 0.75), Nulato (r = 0.62) and Allakaket (r = 0.6) (Appendix D). The remaining eight RIB locations had modest correlations with $MMOD_{PMW}$ averaging 0.42. For these 11 RIB locations, the $MMOD_{PMW}$ occurred 26 days earlier than the RIB. SMD_{PMW} was statistically significant at only four RIB locations, including Russian Mountain (r = 0.52), Circle (r = 0.42), Holy Cross (r = 0.4) and Kaltag (r = 0.36) (Table 3).

Table 3. Snow metrics and RIB regressions mentioned in this section, including significant interactions and correlations. All regression outputs are found in Appendix D.

Station	Metric	Correlation [r]	Pvalue	Observations	Snow Metric [DOY]	Observed RIB [DOY]	Difference [Days]
Allakaket	mmod	0.6	0.001	26	112.5	130.19	−17.69
Beaver	mmod	0.75	0	20	108.2	130.1	−21.9
Nulato	mmod	0.62	0.004	20	98.85	132.35	−33.5
Beaver	snowoff	0.81	0	20	130.2	130.1	0.1
Circle	snowoff	0.63	0	28	131.43	128.71	2.71
Eagle	snowoff	0.63	0	29	135.14	123.66	11.48
Holy Cross	snowoff	0.64	0	26	125.04	134.27	−9.23
Russian Mission	smd	0.52	0.007	26	40.38	134.12	−93.73
Circle	smd	0.42	0.024	28	22.25	128.71	−106.46
Holy Cross	smd	0.4	0.042	26	33.73	134.27	−100.54
Kaltag	smd	0.36	0.07	26	34.27	133.31	−99.04

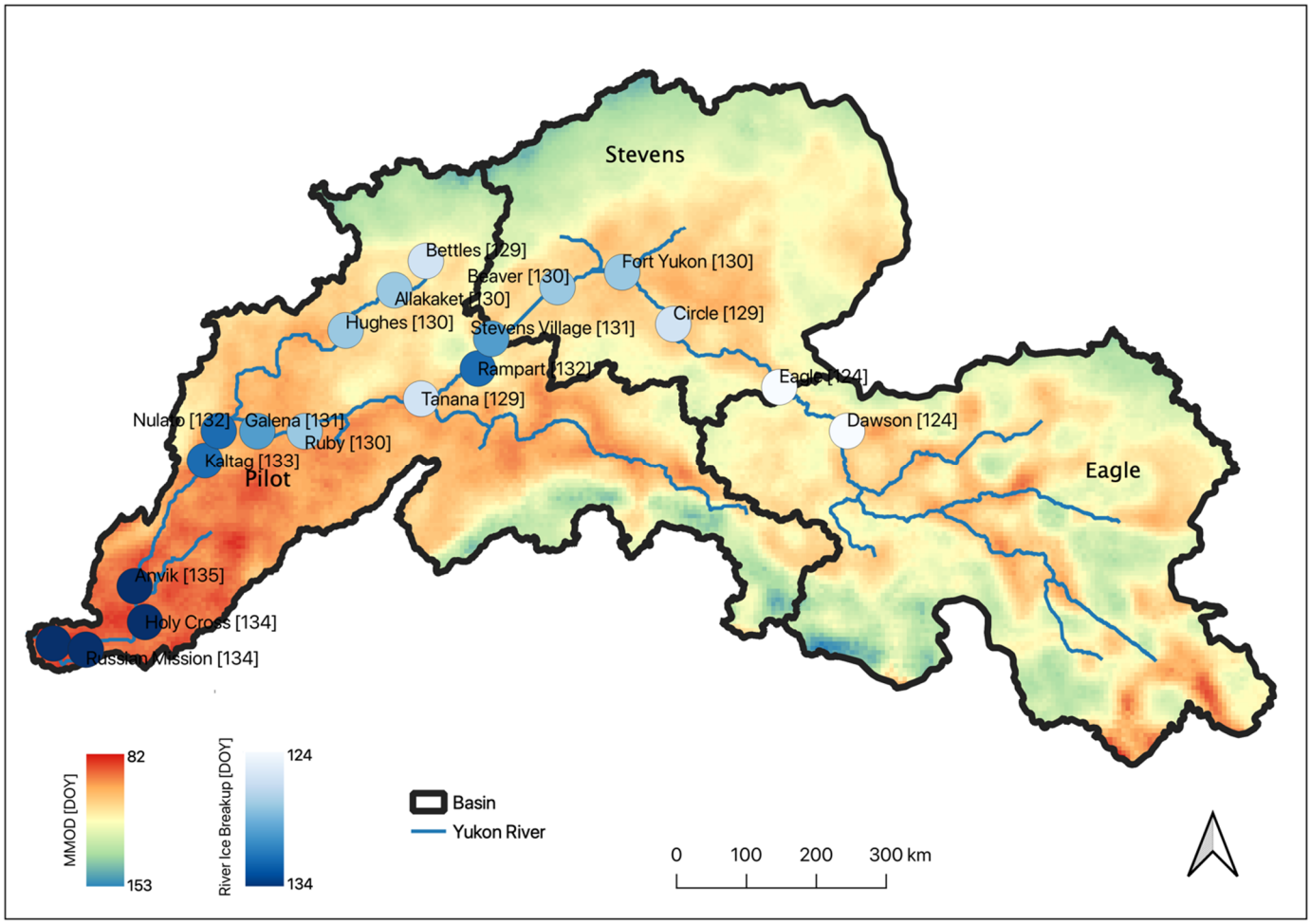

Figure 9. Average RIB date at each of the 19 observation locations in relation to average MMOD derived from the satellite PMW retrievals ($MMOD_{PMW}$) across the YRB from the 1988–2016 record. RIB occurs later at lower elevations and earlier towards the headwater reaches.

The SO_{PMW} snow metric was significantly correlated with RIB timing at all 19 observation locations, with an average correlation of 0.58. Nine of the 19 locations were exceptionally significant ($p < 0.001$), had a mean correlation of 0.71 and ranged between 0.63 (Circle and Eagle) and 0.81 (Beaver). On average for the 19 observation locations, SO_{PMW} occurred less than a day before RIB, although for some sites and years SO_{PMW} preceded RIB by up to nine days (Holy Cross) or followed RIB by up to 11 days (Eagle).

We next examined relations between the timing of the satellite PMW-derived snow metric quantiles and observed RIB on the premise that river ice conditions are responsive to the snowmelt runoff pulse contributed from the surrounding drainage basin. The PMW snow metric quantiles generally showed a stronger relationship with RIB than the streamflow quantiles. RIB timing was significantly correlated with $Q20_{MMOD}$ ($p < 0.01$) and $Q50_{MMOD}$ ($p < 0.05$) in the surrounding catchments at all 19 RIB observation locations. The correlation between $Q20_{MMOD}$ and RIB averaged 0.61 and ranged from 0.48 (Galena) to 0.77 (Bettles) across the 19 RIB observation sites. At the 19 RIB locations, $Q20_{MMOD}$ occurred an average of 27 days before the RIB. At the Bettles station, $Q20_{MMOD}$ occurred only eight days before RIB on average, while $Q20_{MMOD}$ preceded RIB by an average of 35 days at the Pilot station. The correlation between $Q50_{MMOD}$ and RIB was slightly lower than for $Q20_{MMOD}$ but still significant, ranging from 0.37 (Eagle) to 0.79 (Allakaket). As expected, the temporal window between $Q50_{MMOD}$ and RIB dates was narrower than for $Q20_{MMOD}$, with $Q50_{MMOD}$ preceding RIB by an average of only 16 days throughout the YRB (Table 4).

Table 4. Selected regressions outputs between snow metric quantiles and RIB.

Snow Metric	Basin	Correlation [r]	Pvalue	Observations	Mean RIB [DOY]	Mean Snow Metric [DOY]
mmodq20	Bettles	0.77	0	29	129	121
mmodq20	Galena	0.48	0.008	29	131	102
mmodq50	Allakaket	0.79	0	26	130	122
mmodq50	Eagle	0.37	0.051	29	124	115
Contribution Peak	Allakaket	0.78	0	26	130	133
Contribution Peak	Bettles	0.75	0	29	129	139
Contribution Peak	Dawson	0.5	0.005	29	124	128
Contribution Peak	Eagle	0.43	0.021	29	124	128
Contribution Peak	Hughes	0.81	0	24	130	131

$Q20_{SO}$ was the strongest correlated snow metric to RIB and significant at all RIB locations, with a mean correlation of 0.77. There were also strong interactions with the other SO quantiles, but correlations diminished as quantiles increased. However, we again found the annual mean difference between $Q20_{SO}$ and RIB to occur within a day of each other, while the other SO quantiles occurred, on average, after RIB. Hence, the potential for the satellite-derived SO metric in forecasting RIB is limited.

In addition to quantiles, we also derived a Contributing Peak metric defined as the date at which the most grid cells in each catchment had begun melting, as indicated from the $MMOD_{PMW}$ retrievals, but where the snowpack had not yet fully depleted (identified by SO_{PMW}). We found the Contributing Peak to be a strong indicator of RIB, showing significant ($p < 0.05$) relationships at all RIB locations, and with a mean correlation of 0.67. The Contributing Peak occurred after the RIB date at only five locations (Allakaket, Bettles, Dawson, Eagle, and Hughes). For the remaining 14 locations, the Contributing Peak occurred an average of seven days before RIB.

4. Discussion

4.1. MMOD Algorithm Performance

The $MMOD_{PMW}$ retrieval method performed favorably in relation to independent SWE and temperature measurement-based MMOD estimates from in situ SNOTEL sites distributed across Alaska. There was an overall stronger mean relationship between $MMOD_{PMW}$ and $MMOD_T$ ($r = 0.69$, bias = −1 day) than with $MMOD_{SWE}$ ($r = 0.49$, bias = −3.63 days). The stronger temperature relationship was attributed to generally greater spatial and temporal heterogeneity in the in situ SWE measurements relative to air temperature, which can propagate to greater uncertainty in identifying the MMOD signal. The satellite retrievals may also falsely classify $MMOD_{PMW}$ in response to early season temporary melt events in lieu of the actual seasonal melt signal [22,47]. Our results identified the weakest correspondence with air temperature in the maritime regions and a strong correlation between the temperature bias and FW ($r = -0.77$, $p < 0.1$). This FW interaction in the maritime region suggests that enhanced regional moisture, such as rain-on-snow, can adversely affect the GRP algorithm performance [24]. Future work should address a more comprehensive approach to distinguish between rain-on-snow and early season melt events from the MMOD [24,46].

While the $MMOD_{PMW}$ retrievals showed generally less correspondence with $MMOD_{SWE}$ than $MMOD_T$, we found SWE bias to be modestly correlated to FF in the Tundra/Taiga ($r = -0.61$, $p < 0.1$) and FW in both the Tundra/Taiga ($r = -0.86$, $p < 0.1$) and Alpine/Prairie ($r = -0.74$, $p < 0.1$). These results suggest $MMOD_{PMW}$ to be most strongly sensitive to the change in surface wetness conditions during seasonal transitions. Further, vegetation biomass contribution to the landscape freeze-thaw (FT) signal can inflate $MMOD_{PMW}$ errors where the timing of the vegetation canopy seasonal FT transition differs from the surrounding snow cover [42]. In more densely vegetated areas, we would expect to see much less direct snow signal and more vegetation FT signal [28,47]. Vegetation cover can also influence snowpack spatial heterogeneity and representativeness

of in situ SNOTEL SWE measurements relative to the surrounding satellite footprint; thus, contributing to larger satellite-site differences [23].

4.2. Changes in Snowmelt Properties

We initially examined long-term trends in snowmelt properties across the YRB from 1988–2016 but found no temporally or spatially consistent patterns despite an overall declining trend in snow cover extent across the Northern Hemisphere [48,49]. Yet, our results indicate that both $MMOD_{PMW}$ and SO_{PMW} occur earlier during anomalously warm years and, conversely, occur later during cooler years. This identified interaction between temperature and snow metrics is very important, as Alaska has experienced several annual temperature records broken over the last few years [43]. With anticipated warming, future lines of research should focus on how these snow metrics can inform the intensity of oncoming wildfire seasons, wildlife movements and ecosystem productivity.

4.3. Snow and Hydrologic Interactions

We found significant relationships ($p < 0.01$) between the satellite-derived snowmelt quantiles and the spring flood pulse indicated from in situ streamflow measurements within the major YRB catchments. Yet, the timing of $Q50_{SO}$ and $Q80_{SO}$ generally showed the strongest correspondence with the streamflow quantiles (Q20, Q50) but occurred after these events, degrading their forecast potential. The day of peak flow is used here to represent the spring flood pulse in the YRB and was strongly correlated to $Q50_{SO}$ at Stevens Village ($r = 0.71$) and Pilot ($r = 0.63$). The peak flow consistently occurred after the $Q50_{SO}$, on average 16, 9, and 17 days earlier than the peak flow for Eagle, Stevens Village, and Pilot, respectively. We would anticipate a smaller lag time at Eagle; however, the associated stream gage station has relatively high interannual variability and showed a weak correlation to $Q20_{SO}$ ($r = 0.21$). Regardless, other studies have placed greater importance on MMOD in understanding the timing of the Spring flood pulse [8,50], although our results indicate that SO quantiles are stronger predictors of peak flow in the YRB. Additional research can benefit by exploring a lower quantile to identify further relationships between snow metrics and their forecasting potential.

A novel component of this study was the derivation of the Contributing Peak metric, derived using MMOD and SO. This metric effectively defines the area that is actively melting, or not melting, across a basin. Of the 19 RIB locations, strong relationships between RIB and Contributing Peak were identified at 11 stations, with a mean correlation of 0.67. At the 11 locations, the Contributing Peak occurred seven days before the RIB on average. Hence, the strong correlation and occurrence before RIB, indicate the Contributing Peak as having forecasting potential. There were five stations (Allakaket, Bettles, Dawson, Eagle, and Hughes) where RIB occurred before the day of Contributing Peak. These stations all exist at the higher elevations, where we also noted RIB occurs earlier relative to the lower elevations. This likely indicates other driver, other than snowmelt, governing RIB.

Our ground observations identified an earlier RIB date in the upper reaches of the Yukon, relative to the lower reaches. These results are in line with other large rivers including the Mackenzie and Yenisey. However, for large high-latitude rivers flowing north, latitude plays a prominent role in an earlier RIB date in southern reaches relative to northern. As the YRB trends from east to west, the influence of latitude is minimized in favor of river channel characteristics such as slope, curvature and other channel-scale factors [51]. The amount of SWE and rate of warming/melting in the catchment, freeze/thaw status and moisture holding capacity of underlying soils also influences the magnitude and rate of melt pulse to rivers affecting the RIB [51,52]. Our satellite-derived snow metrics did not fully capture these additional factors, which may degrade the observed correspondence with discharge and RIB.

The satellite-derived snow metrics developed here have several intrinsic limitations. The moderate spatial resolution (6.25 km) captures the overall latitudinal and altitudinal patterns across the domain. However, a significant amount of landscape heterogeneity

exists within each pixel, which influences algorithm performance. Currently, the snow metrics capture the timing of snow processes rather than amount of melt. Hence, the snow metrics lack a representation of SWE and snowmelt rates controlling runoff magnitude, routing and soil storage influencing discharge. The strength of the snow metrics resides in the use of daily Tb observations and their strong sensitivity to the rapid changes in surface wetness from snowmelt.

5. Conclusions

The seasonal and spatial timing in snowmelt properties are important controls on ecosystem and socioeconomic processes across Arctic boreal landscapes, including the YRB. However, capabilities for regional monitoring of snow phenology and its influence on the spring flood pulse and RIB are constrained by the sparse in situ station observation network and limited satellite resources. In this study, we presented a new satellite PMW MMOD retrieval method and dataset that exploits the differential response between 19V and 37V GHz Tb channels with daily repeat and 6.25 km resolution gridding from 1988 to 2016 over the YRB. The developed algorithm is physically-based, drawing from the established GRP method and incorporating a dynamic detection threshold adjusted according to surface FW cover. The $MMOD_{PMW}$ results compared favorably with the regional pattern and annual variability in the primary spring thaw signal from the FT-ESDR occurring about five days later. The $MMOD_{PMW}$ retrievals also showed favorable agreement with independent in situ SWE (r = 0.49, bias = −3.6 days) and air temperature (r = 0.69, bias = 1 day) measurement based MMOD estimates from the regional weather station network. The regional pattern in $MMOD_{PMW}$ performance was influenced by one or more landscape factors, including the prevailing climate and snow type, terrain complexity, forest cover (FF) and the fractional open water body cover (FW) within the satellite footprint.

The resulting satellite snow metrics developed in this study showed that MMOD extends from early March into early June across the YRB. Melt begins at lower elevations and reaches of the Yukon before progressing inland and into higher elevations of the upper YRB reaches. SO timing followed a similar pattern to MMOD, but with a delayed response, where SO generally occurred in March in the YRB coastal areas and lower elevations, and extended as late as July in the higher elevations and upper reaches of the basin. The SMD was generally longer where MMOD and SO occurred earlier. Conversely, SMD was the shortest (<20 days) at higher elevations and in more interior regions. The timing of all snow metrics was sensitive to relatively warm and cool years. For example, both MMOD and SO occurred approximately 12 days and 11 days earlier during the anomalous warm year in 2016, respectively.

Positive and significant regressions were identified between the spring flood pulse and both MMOD and SO. The timing of $Q50_{SO}$ was found to be the best indicator of peak discharge at the Stevens Village and Pilot stations. $Q50_{SO}$ also occurred before peak discharge at both locations, making it one of the better predictors of the spring flood pulse. Overall, regressions were stronger between the snow metrics and RIB, with $Q20_{SO}$ having the best correlation at all stations. However, for all stations, on average, $Q20_{SO}$ occurred within one day of the RIB, limiting its potential utility as a forecast indicator. The $Q20_{MMOD}$ and $Q50_{MMOD}$ metrics indicated stronger potential utility as early predictors of seasonal ice breakup in the YRB, showing strong correlations with RIB and preceding seasonal ice breakup by approximately 35 days and 16 days, respectively. Yet, the Contributing Peak possessed the strongest correlations and occurred seven days on average before RIB at 11 of the 19 locations.

Anomalously warm years like 2016, when the cold season temperatures were + 4 °C above normal, coincided with MMOD and SO timing that was more than 10 days earlier than normal. This interaction indicates that the snow metrics accurately reflect seasonal surface air temperature conditions represented from regional reanalysis data, which is congruent with other studies [51,53]. Hence, projected regional warming trends of approximately 1–3 °C in spring air temperatures by midcentury [9,54] are expected to promote

generally earlier onset of MMOD and SO across the YRB, along with generally earlier ice breakup and earlier onset of the spring flood pulse. Such changes in snow and hydrologic processes will affect fluvial dynamics and fisheries, as well as terrestrial processes like spring carbon uptake and wildfires, making further research at the intersection of snow and ecologic processes of high value.

Author Contributions: C.G.P., P.B.K. and J.S.K. designed the study; C.G.P., P.B.K. and J.D., analyzed the data; all authors contributed to the writing and editing. All authors have read and agreed to the published version of the manuscript.

Funding: This research was funded by the National Park Service Southwest Alaska, NASA grants (80NSSC19K0649, 80NSSC19M0114) in support of the Arctic Boreal Vulnerability Experiment (ABoVE).

Institutional Review Board Statement: Not Applicable.

Informed Consent Statement: Not Applicable.

Data Availability Statement: Snow metrics are available for free at the Oak Ridge National LaboratoryLPDAAC. The DOIs for MMOD, SO, and SMD are as follows, 10.334/ORNLDAAC/1843, 10.334/ORNLDAAC/1841, and 10.3334/ORNLDAAC/1711.

Acknowledgments: We thank three anonymous reviewers for their thoughtful and constructive comments.

Conflicts of Interest: The authors declare no conflict of interest.

Appendix A

Table A1. SNOTEL validation stations used in this study. FW is fractional cover. FF is forest fraction.

Name	Period of Record		Latitude	Longitude	FW [%]	FF [%]
	Start	End				
ANCHOR RIVER DIVIDE	2007	2020	59.86	−151.32	23.17	20
BETTLES FIELD	2011	2020	66.92	−151.53	0.81	19
COLDFOOT	2003	2020	67.25	−150.18	0.60	15
FAIRBANKS F.O.	2011	2020	64.85	−147.80	1.11	11
GRANITE CRK	2003	2020	63.94	−145.40	1.83	37
GRANDVIEW	2003	2020	60.61	−149.06	8.70	48
INDEPENDENCE MINE	2007	2020	61.79	−149.28	3.79	0
KENAI MOOSE PENS	2003	2020	60.73	−150.48	31.02	45
LITTLE CHENA RIDGE	2003	2020	65.12	−146.73	0.34	14
MONUMENT CREEK	2003	2020	65.08	−145.87	0.26	3
MUNSON RIDGE	2003	2020	64.85	−146.21	0.22	4
MT. RYAN	2003	2020	65.25	−146.15	0.30	5
POINT MACKENZIE	2003	2015	61.39	−150.03	17.84	33
MAY CREEK	2009	2020	61.35	−142.71	4.05	55
SUMMIT CREEK	2003	2020	60.62	−149.53	7.28	31
SUSITNA VALLEY HIGH	2003	2020	62.13	−150.04	2.34	34
TEUCHET CREEK	2003	2020	64.95	−145.52	0.23	29
TOKOSITNA VALLEY	2007	2020	62.63	−150.78	3.35	35
TURNAGAIN PASS	2003	2020	60.78	−149.18	10.37	24
UPPER TSAINA RIVER	2009	2020	61.19	−145.65	5.59	4

Appendix B

Table A2. River Ice breakup observation information in this analysis acquired from the GRDC.

Location	Longitude [dd]	Latitude [dd]	Start	End	Obs	Basin
Koyukuk River at Allakaket	−152.64	66.57	1988	2017	28	Pilot
Koyukuk River at Bettles	−151.51	66.93	1988	2017	30	Pilot
Koyukuk River at Hughes	−154.26	66.05	1988	2017	25	Pilot
Yukon River at Anvik	−160.19	62.66	1988	2017	28	Pilot
Yukon River at Beaver	−147.39	66.36	1997	2017	21	Stevens

Table A2. *Cont.*

Location	Longitude [dd]	Latitude [dd]	Start	End	Obs	Basin
Yukon River at Circle	−144.06	65.83	1988	2017	29	Stevens
Yukon River at Dawson	−139.43	64.07	1988	2017	30	Eagle
Yukon River at Eagle	−141.33	64.79	1988	2017	30	Eagle
Yukon River at Fort Yukon	−145.28	66.56	1988	2017	29	Stevens
Yukon River at Galena	−156.9	64.74	1988	2017	30	Pilot
Yukon River at Holy Cross	−159.77	62.21	1988	2017	28	Pilot
Yukon River at Kaltag	−158.73	64.33	1988	2017	27	Pilot
Yukon River at Marshall	−162.09	61.88	1988	2017	21	Pilot
Yukon River at Nulato	−158.1	64.72	1997	2017	21	Pilot
Yukon River at Rampart	−150.17	65.51	1996	2017	20	Pilot
Yukon River at Ruby	−155.48	64.74	1988	2017	30	Pilot
Yukon River at Russian Mission	−161.32	61.78	1988	2017	28	Pilot
Yukon River at Stevens Village	−149.72	65.88	1998	2017	18	Stevens
Yukon River at Tanana	−152.07	65.17	1988	2017	28	Pilot

Appendix C

Table A3. Snowmelt and hydrologic regression outputs at each catchment. Correlation values are only calculated for statistically significant relationships.

Snow Variable	Meanr	Minr	Maxr	Significant Variables	Basin
Contribution Peak	0.565	0.55	0.58	['Peak', 'Q20 ']	PILOT
MMOD Q50	0.41	0.4	0.42	['Peak', 'Q20 ']	PILOT
MMOD Q80	0.49	0.4	0.58	['Peak', 'Q20 ']	PILOT
SO Q20	0.5	0.48	0.52	['Peak', 'Q20 ']	PILOT
SO Q50	0.59	0.55	0.63	['Peak', 'Q20 ']	PILOT
SO Q80	0.47	0.47	0.47	['Peak']	PILOT
Contribution Peak	0.655	0.64	0.67	['Peak', 'Q20 ']	STEVENS VILLAGE
MMOD Peak	0.455	0.4	0.51	['Peak', 'Q20 ']	STEVENS VILLAGE
MMOD Q20	0.39	0.37	0.41	['Peak', 'Q20 ']	STEVENS VILLAGE
MMOD Q50	0.58	0.58	0.58	['Peak', 'Q20 ']	STEVENS VILLAGE
MMOD Q80	0.68	0.65	0.71	['Peak', 'Q20 ']	STEVENS VILLAGE
SO Peak	0.475	0.38	0.57	['Peak', 'Q20 ']	STEVENS VILLAGE
SO Q20	0.675	0.67	0.68	['Peak', 'Q20 ']	STEVENS VILLAGE
SO Q50	0.675	0.64	0.71	['Peak', 'Q20 ']	STEVENS VILLAGE
SO Q80	0.59	0.52	0.66	['Peak', 'Q20 ']	STEVENS VILLAGE
Contribution Peak	0.6	0.6	0.6	['Q20 ']	EAGLE
MMOD Q20	0.5	0.5	0.5	['Q20 ']	EAGLE
MMOD Q50	0.48	0.48	0.48	['Q20 ']	EAGLE
MMOD Q80	0.47	0.47	0.47	['Q20 ']	EAGLE
SO Q20	0.61	0.61	0.61	['Q20 ']	EAGLE
SO Q50	0.49	0.49	0.49	['Q20 ']	EAGLE
SO Q80	0.46	0.46	0.46	['Q20 ']	EAGLE

Appendix D

Table A4. Snowmelt and RIB regression outputs at each RIB observation location.

Station	Metric	Cor	Pval	Nobs	Meansnow	Meanri	Dif
Koyukuk River at Allakaket	mmod	0.6	0.001	26	112.50	130.19	−17.69
Koyukuk River at Bettles	mmod	0.42	0.023	29	109.72	129.38	−19.66
Koyukuk River at Hughes	mmod	0.36	0.085	24	106.67	130.08	−23.42
Yukon River at Anvik	mmod	0.42	0.035	25	91.92	135.00	−43.08
Yukon River at Beaver	mmod	0.75	0	20	108.20	130.10	−21.90
Yukon River at Circle	mmod	0.12	0.559	28	111.00	128.71	−17.71
Yukon River at Dawson	mmod	0.4	0.034	29	110.48	123.97	−13.48
Yukon River at Eagle	mmod	0.45	0.014	29	111.83	123.66	−11.83
Yukon River at Fort Yukon	mmod	0.15	0.457	28	105.00	129.50	−24.50
Yukon River at Galena	mmod	0.41	0.029	29	101.79	131.34	−29.55
Yukon River at Holy Cross	mmod	0.46	0.018	26	91.73	134.27	−42.54

Table A4. *Cont.*

Station	Metric	Cor	Pval	Nobs	Meansnow	Meanri	Dif
Yukon River at Kaltag	mmod	0.17	0.396	26	94.00	133.31	−39.31
Yukon River at Marshall	mmod	0.34	0.141	20	91.40	134.45	−43.05
Yukon River at Nulato	mmod	0.62	0.004	20	98.85	132.35	−33.50
Yukon River at Rampart	mmod	0.36	0.125	19	112.89	131.79	−18.89
Yukon River at Ruby	mmod	0.48	0.019	24	97.38	130.04	−32.67
Yukon River at Russian Mission	mmod	0.25	0.214	26	85.42	134.12	−48.69
Yukon River at Stevens Village	mmod	0.32	0.217	17	111.94	130.88	−18.94
Yukon River at Tanana	mmod	0.11	0.596	25	102.60	128.88	−26.28
Koyukuk River at Allakaket	smd	−0.02	0.929	26	22.88	130.19	−107.31
Koyukuk River at Bettles	smd	0.18	0.346	29	24.86	129.38	−104.52
Koyukuk River at Hughes	smd	−0.03	0.881	24	24.96	130.08	−105.13
Yukon River at Anvik	smd	0.18	0.384	25	33.88	135.00	−101.12
Yukon River at Beaver	smd	−0.25	0.292	20	22.35	130.10	−107.75
Yukon River at Circle	smd	0.42	0.024	28	22.25	128.71	−106.46
Yukon River at Dawson	smd	−0.15	0.43	29	21.76	123.97	−102.21
Yukon River at Eagle	smd	0.05	0.792	29	22.31	123.66	−101.34
Yukon River at Fort Yukon	smd	0.16	0.424	28	24.36	129.50	−105.14
Yukon River at Galena	smd	−0.21	0.279	29	27.69	131.34	−103.66
Yukon River at Holy Cross	smd	0.4	0.042	26	33.73	134.27	−100.54
Yukon River at Kaltag	smd	0.36	0.07	26	34.27	133.31	−99.04
Yukon River at Marshall	smd	0.16	0.51	20	35.55	134.45	−98.90
Yukon River at Nulato	smd	−0.05	0.82	20	33.35	132.35	−99.00
Yukon River at Rampart	smd	0.21	0.381	19	21.21	131.79	−110.58
Yukon River at Ruby	smd	0.01	0.973	24	29.29	130.04	−100.75
Yukon River at Russian Mission	smd	0.52	0.007	26	40.38	134.12	−93.73
Yukon River at Stevens Village	smd	0.17	0.511	17	21.41	130.88	−109.47
Yukon River at Tanana	smd	−0.08	0.696	25	24.96	128.88	−103.92
Koyukuk River at Allakaket	snowoff	0.78	0	26	134.08	130.19	3.88
Koyukuk River at Bettles	snowoff	0.7	0	29	134.66	129.38	5.28
Koyukuk River at Hughes	snowoff	0.48	0.018	24	131.38	130.08	1.29
Yukon River at Anvik	snowoff	0.7	0	25	125.40	135.00	−9.60
Yukon River at Beaver	snowoff	0.81	0	20	130.20	130.10	0.10
Yukon River at Circle	snowoff	0.63	0	28	131.43	128.71	2.71
Yukon River at Dawson	snowoff	0.5	0.006	29	131.69	123.97	7.72
Yukon River at Eagle	snowoff	0.63	0	29	135.14	123.66	11.48
Yukon River at Fort Yukon	snowoff	0.34	0.08	28	130.93	129.50	1.43
Yukon River at Galena	snowoff	0.42	0.025	29	129.07	131.34	−2.28
Yukon River at Holy Cross	snowoff	0.64	0	26	125.04	134.27	−9.23
Yukon River at Kaltag	snowoff	0.54	0.005	26	127.85	133.31	−5.46
Yukon River at Marshall	snowoff	0.39	0.093	20	126.00	134.45	−8.45
Yukon River at Nulato	snowoff	0.73	0	20	133.75	132.35	1.40
Yukon River at Rampart	snowoff	0.59	0.008	19	135.05	131.79	3.26
Yukon River at Ruby	snowoff	0.54	0.007	24	127.25	130.04	−2.79
Yukon River at Russian Mission	snowoff	0.46	0.017	26	125.81	134.12	−8.31
Yukon River at Stevens Village	snowoff	0.73	0.001	17	132.00	130.88	1.12
Yukon River at Tanana	snowoff	0.5	0.011	25	124.48	128.88	−4.40

Appendix E

Table A5. List of abbreviations.

Abbreviation	Description
MMOD	Main Melt Onset Date
SMD	Snow Melt Duration
SO	Snowoff Date
PMW	Passive Microwave
$MMOD_{PMW}$	MMOD derived from passive microwave observations
SMD_{PMW}	SMD derived from passive microwave observations
SO_{PMW}	SO derived from passive microwave observations
RIB	River ice breakup date

Table A5. *Cont.*

Abbreviation	Description
LWC	Liquid water content
Tb	Brightness temperature
GRP	Gradient Ratio Polarization
YRB	Yukon River Basin
DMSP	Defense Meteorological Satellite Program
NOAA	National Oceanic and Atmospheric Administration
SSM/I	Special Sensor Microwave/Imager
km	Kilometer
Ghz	Gigahertz
H	Horizontal
V	Vertical
MEaSUREs	Making Earth Data Systems Data Records for Use in Research
WY	Water year
FW	Fractional water
SNOTEL	Snow Telemetry
$MMOD_T$	MMOD detected from SNOTEL temperature
$MMOD_{SWE}$	MMOD detected from SNOTEL SWE
FT	Freeze/Thaw
GRDC	Global Runoff Database Centre
Q	Quantiles
DOY	Day of year
GLIMS	Global Land Ice Measurements from Space
JJA	June July August
AMSR	Advanced Microwave Scanning Radiometer
SNAP	Scenarios Network for Alaska and Arctic Planning
MODIS	Moderate Resolution Imaging Spectroradiometer
FF	Fractional Forest
$Q20_{MMOD}$	MMOD Q20
$Q20_{Flow}$	Quantile derived from streamflow
$Q20_{SO}$	SO Q20

References

1. Barnhart, T.B.; Molotch, N.P.; Livneh, B.; Harpold, A.A.; Knowles, J.F.; Schneider, D. Snowmelt rate dictates streamflow. *Geophys. Res. Lett.* **2016**, *43*, 8006–8016. [CrossRef]
2. Clow, D.W. Changes in the timing of snowmelt and streamflow in Colorado: A response to recent warming. *J. Clim.* **2010**, *23*, 2293–2306. [CrossRef]
3. Pederson, G.T.; Gray, S.T.; Ault, T.; Marsh, W.; Fagre, D.B.; Bunn, A.G.; Woodhouse, C.A.; Graumlich, L.J. Climatic controls on the snowmelt hydrology of the northern Rocky Mountains. *J. Clim.* **2011**, *24*, 1666–1687. [CrossRef]
4. Adam, J.; Hamlet, A.; Lettenmaier, D. Implications of global climate change for snowmelt hydrology in the twenty-first century. *Hydrol. Process.* **2009**, *23*, 962–972. [CrossRef]
5. Musselman, K.N.; Clark, M.P.; Liu, C.; Ikeda, K.; Rasmussen, R. Slower snowmelt in a warmer world. *Nat. Clim. Chang.* **2017**, *7*, 214–220. [CrossRef]
6. Beltaos, S.; Prowse, T. River-ice hydrology in a shrinking cryosphere. *Hydrol. Process.* **2009**, *23*, 122–144. [CrossRef]
7. Lesack, L.F.W.; Marsh, P.; Hicks, F.E.; Forbes, D.L. Local spring warming drives earlier river-ice breakup in a large Arctic Delta. *Geophys. Res. Lett.* **2014**, *41*, 1560–1566. [CrossRef]
8. Semmens, K.A.; Ramage, J.M. Recent changes in spring snowmelt timing in the Yukon River basin detected by passive microwave satellite data. *Cryosph.* **2013**, *7*, 905–916. [CrossRef]
9. Cold, H.S.; Brinkman, T.J.; Brown, C.L.; Hollingsworth, T.N.; Brown, D.R.N.; Heeringa, K.M. Assessing vulnerability of subsistence travel to effects of environmental change in interior Alaska. *Ecol. Soc.* **2020**, *25*. [CrossRef]
10. Brown, D.R.N.; Brinkman, T.J.; Bolton, W.R.; Brown, C.L.; Cold, H.S.; Hollingsworth, T.N.; Verbyla, D.L. Implications of climate variability and changing seasonal hydrology for subarctic riverbank erosion. *Clim. Change* **2020**. [CrossRef]
11. Rokaya, P.; Budhathoki, S.; Lindenschmidt, K.E. Trends in the Timing and Magnitude of Ice-Jam Floods in Canada. *Sci. Rep.* **2018**, *8*, 1–9. [CrossRef]
12. Callaghan, T.V.; Johansson, M.; Brown, R.D.; Groisman, P.Y.; Labba, N.; Radionov, V.; Barry, R.G.; Bulygina, O.N.; Essery, R.L.H.; Frolov, D.M.; et al. The Changing Face of Arctic Snow Cover: A Synthesis of Observed and Projected Changes. *Ambio* **2012**, 17–31. [CrossRef]

13. Serreze, M.C.; Barry, R.G. Process and impacts of Arctic amplification: A research synthesis. *Glob. Planet. Change* **2011**, *77*, 85–96. [CrossRef]
14. Bieniek, P.A.; Walsh, J.E.; Thoman, R.L.; Bhatt, U.S. Using climate divisions to analyze variations and trends in Alaska temperature and precipitation. *J. Clim.* **2014**, *27*, 2800–2818. [CrossRef]
15. Boelman, N.T.; Liston, G.E.; Gurarie, E.; Meddens, A.J.H.; Mahoney, P.J.; Kirchner, P.B.; Bohrer, G.; Brinkman, T.J.; Cosgrove, C.L.; Eitel, J.U.H.; et al. Integrating snow science and wildlife ecology in Arctic-boreal North America. *Environ. Res. Lett.* **2019**, *14*. [CrossRef]
16. Naderpour, R.; Houtz, D.; Schwank, M. Snow wetness retrieved from close-range L-band radiometry in the western Greenland ablation zone. *J. Glaciol.* **2021**, *67*, 27–38. [CrossRef]
17. Houtz, D.; Mätzler, C.; Naderpour, R.; Schwank, M.; Steffen, K. Quantifying Surface Melt and Liquid Water on the Greenland Ice Sheet using L-band Radiometry. *Remote Sens. Environ.* **2021**, *256*. [CrossRef]
18. Du, J.; Kimball, J.S.; Jones, L.A.; Kim, Y.; Glassy, J.; Watts, J.D. A global satellite environmental data record derived from AMSR-E and AMSR2 microwave Earth observations. *Earth Syst. Sci. Data* **2017**, *9*, 791–808. [CrossRef]
19. Tedesco, M.; Derksen, C.; Deems, J.S.; Foster, J.L. Remote sensing of snow depth and snow water equivalent. *Remote Sens. Cryosph.* **2015**, 73–98. [CrossRef]
20. Tedesco, M.; Miller, J. Observations and statistical analysis of combined active-passive microwave space-borne data and snow depth at large spatial scales. *Remote Sens. Environ.* **2007**, *111*, 382–397. [CrossRef]
21. Ramage, J.M.; Isacks, B.L. Determination of melt-onset and refreeze timing on southeast Alaskan icefields using SSM/I diurnal amplitude variations. *Ann. Glaciol.* **2002**, *34*, 391–398. [CrossRef]
22. Wang, L.; Toose, P.; Brown, R.; Derksen, C. Frequency and distribution of winter melt events from passive microwave satellite data in the pan-Arctic, 1988-2013. *Cryosphere* **2016**, *10*, 2589–2602. [CrossRef]
23. Kim, Y.; Kimball, J.S.; Glassy, J.; Du, J. An extended global Earth system data record on daily landscape freeze – thaw status determined from satellite passive microwave remote sensing. *Earch Syst. Sci. Data* **2017**, *9*, 133–147. [CrossRef]
24. Pan, C.G.; Kirchner, P.B.; Kimball, J.S.; Kim, Y.; Du, J. Rain-on-snow events in Alaska, their frequency and distribution from satellite observations. *Environ. Res. Lett.* **2018**, *13*. [CrossRef]
25. Pan, C.G.; Kimball, J.S.; Munkhjargal, M.; Robinson, N.P.; Tijdeman, E.; Menzel, L.; Kirchner, P.B. Role of Surface Melt and Icing Events in Livestock Mortality across Mongolia's Semi-Arid Landscape. *Remote Sens.* **2019**, *11*, 2392. [CrossRef]
26. Takala, M.; Luojus, K.; Pulliainen, J.; Derksen, C.; Lemmetyinen, J.; Kärnä, J.P.; Koskinen, J.; Bojkov, B. Estimating northern hemisphere snow water equivalent for climate research through assimilation of space-borne radiometer data and ground-based measurements. *Remote Sens. Environ.* **2011**, *115*, 3517–3529. [CrossRef]
27. Lindsay, C.; Zhu, J.; Miller, A.E.; Kirchner, P.; Wilson, T.L. Deriving snow cover metrics for Alaska from MODIS. *Remote Sens.* **2015**, *7*, 12961–12985. [CrossRef]
28. Pan, C.G.; Kirchner, P.B.; Kimball, J.S.; Du, J. A Long-Term Passive Microwave Snowoff Record for the Alaska Region 1988 – 2016. *Remote Sens.* **2020**, *12*, 153. [CrossRef]
29. Steiner, N.; Tedesco, M. A wavelet melt detection algorithm applied to enhanced-resolution scatterometer data over Antarctica (2000-2009). *Cryosphere* **2014**, *8*, 25–40. [CrossRef]
30. Kim, Y.; Kimball, J.S.; Robinson, D.A.; Derksen, C. New satellite climate data records indicate strong coupling between recent frozen season changes and snow cover over high northern latitudes. *Environ. Res. Lett.* **2015**, *10*, 1–10. [CrossRef]
31. Rawlins, M.A.; McDonald, K.C.; Frolking, S.; Lammers, R.B.; Fahnestock, M.; Kimball, J.S.; Vörösmarty, C.J. Remote sensing of snow thaw at the pan-Arctic scale using the SeaWinds scatterometer. *J. Hydrol.* **2005**, *312*, 294–311. [CrossRef]
32. Brabets, T.P.; Wang, B.; Meade, R.H. Environmental and hydrologic overview of the Yukon River basin, Alaska and Canada. *USGS Water-Resources Investig. Rep.* **2000**, *99*, 1–114.
33. Brodzik, M.J.; Long, D.G.; Harman, A.; Page, A.; Armstong, R. Updated 2020. MEaSUREs Calibrated Enhanced-Resolution Passive Microwave Daily EASE-Grid 2.0 Brightness Temperature ESDR, Version 1. Available online: https://nsidc.org/data/nsidc-0630/versions/1 (accessed on 30 August 2020).
34. Long, D.G.; Brodzik, M.J. Optimum Image Formation for Spaceborne Microwave Radiometer Products. *IEEE Trans. Geosci. Remote Sens.* **2016**, *54*, 2763–2779. [CrossRef] [PubMed]
35. Brodzik, M.; Long, D.; Hardman, M. Best Practices in Crafting the Calibrated, Enhanced-Resolution Passive-Microwave EASE-Grid 2.0 Brightness Temperature Earth System Data Record. *Remote Sens.* **2018**, *10*, 1793. [CrossRef]
36. Du, J.; Kimball, J.S.; Jones, L.A.; Watts, J.D. Implementation of satellite based fractional water cover indices in the pan-Arctic region using AMSR-E and MODIS. *Remote Sens. Environ.* **2016**, *184*, 469–481. [CrossRef]
37. Carroll, M.; Townshend, J.; Hansen, M.; DiMiceli, C.; Sohlberg, R.; Wurster, K. MODIS Vegetative Cover Conversion and Vegetation Continuous Fields BT - Land Remote Sensing and Global Environmental Change: NASA's Earth Observing System and the Science of ASTER and MODIS. In *Remote Sensing and Digital Image Processing*; Ramachandran, B., Justice, C.O., Abrams, M.J., Eds.; Springer: New York, NY, USA, 2011; pp. 725–745. ISBN 978-1-4419-6749-7.
38. Cai, L.; Alexeev, V.A.; Arp, C.D.; Jones, B.M.; Liljedahl, A.K.; Gädeke, A. The polar WRF downscaled historical and projected twenty-first century climate for the coast and foothills of arctic alaska. *Front. Earth Sci.* **2018**, *5*, 1–15. [CrossRef]
39. Dolant, C.; Langlois, A.; Montpetit, B.; Brucker, L.; Roy, A.; Royer, A. Development of a rain-on-snow detection algorithm using passive microwave radiometry. *Hydrol. Process.* **2016**, *30*, 3184–3196. [CrossRef]

40. Wang, L.; Derksen, C.; Brown, R.; Markus, T. Recent changes in pan-Arctic melt onset from satellite passive microwave measurements. *Geophys. Res. Lett.* **2013**, *40*, 522–528. [CrossRef]
41. Wang, K.; Jafarov, E.; Overeem, I.; Romanovsky, V.; Schaefer, K.; Clow, G.; Urban, F.; Cable, W.; Piper, M.; Schwalm, C.; et al. A synthesis dataset of permafrost-affected soil thermal conditions for Alaska, USA. *Earth Syst. Sci. Data* **2018**, *10*, 2311–2328. [CrossRef]
42. Chen, X.; Liu, L.; Bartsch, A. Detecting soil freeze/thaw onsets in Alaska using SMAP and ASCAT data. *Remote Sens. Environ.* **2019**, *220*, 59–70. [CrossRef]
43. Walsh, J.E.; Bieniek, P.A.; Brettschneider, B.; Euskirchen, E.S.; Lader, R.; Thoman, R.L. The exceptionally warm winter of 2015/16 in Alaska. *J. Clim.* **2017**, *30*, 2069–2088. [CrossRef]
44. Musselman, K.N.; Lehner, F.; Ikeda, K.; Clark, M.P.; Prein, A.F.; Liu, C.; Barlage, M.; Rasmussen, R. Projected increases and shifts in rain-on-snow flood risk over western North America. *Nat. Clim. Chang.* **2018**, *8*. [CrossRef]
45. Wu, X.; Che, T.; Li, X.; Wang, N.; Yang, X. Slower Snowmelt in Spring Along With Climate Warming Across the Northern Hemisphere. *Geophys. Res. Lett.* **2018**, *45*, 12,331–12,339. [CrossRef]
46. Scalzitti, J.; Strong, C.; Kochanski, A. Climate change impact on the roles of temperature and precipitation in western U.S. snowpack variability. *Geophys. Res. Lett.* **2016**, *43*, 5361–5369. [CrossRef]
47. Wang, L.; Derksen, C.; Brown, R. Detection of pan-Arctic terrestrial snowmelt from QuikSCAT, 2000-2005. *Remote Sens. Environ.* **2008**, *112*, 3794–3805. [CrossRef]
48. Derksen, C.; Brown, R. Spring snow cover extent reductions in the 2008-2012 period exceeding climate model projections. *Geophys. Res. Lett.* **2012**, *39*, 1–6. [CrossRef]
49. Dolant, C.; Langlois, A.; Brucker, L.; Royer, A.; Roy, A.; Montpetit, B. Meteorological inventory of rain-on-snow events in the Canadian Arctic Archipelago and satellite detection assessment using passive microwave data. *Phys. Geogr.* **2017**, *3646*, 1–17. [CrossRef]
50. Stewart, I.T.; Cayan, D.R.; Dettinger, M.D. Changes in snowmelt runoff timing using a 'business as usual' climate change scenario. *Clim. Change* **2004**, *62*, 217–232. [CrossRef]
51. Pavelsky, T.M.; Smith, L.C. Spatial and temporal patterns in Arctic river ice breakup observed with MODIS and AVHRR time series. *Remote Sens. Environ.* **2004**, *93*, 328–338. [CrossRef]
52. Bormann, K.J.; Brown, R.D.; Derksen, C.; Painter, T.H. Estimating snow-cover trends from space. *Nat. Clim. Chang.* **2018**, *8*, 924–928. [CrossRef]
53. Park, H.; Yoshikawa, Y.; Oshima, K.; Kim, Y.; Ngo-Duc, T.; Kimball, J.S.; Yang, D. Quantification of warming climate-induced changes in terrestrial Arctic river ice thickness and phenology. *J. Clim.* **2016**, *29*, 1733–1754. [CrossRef]
54. Bieniek, P.A.; Bhatt, U.S.; Rundquist, L.A.; Lindsey, S.D.; Zhang, X.; Thoman, R.L. Large-scale climate controls of interior Alaska river ice breakup. *J. Clim.* **2011**, *24*, 286–297. [CrossRef]